

Electronic Supplementary Information

Mode-dependent energy exchange between near- and far-field through silicon-supported single silver nanorods

Xiaolu Zhuo,^{*‡ab} Shasha Li,^{‡a} Nannan Li,^{‡a} Xizhe Cheng,^a Yunhe Lai^a and Jianfang Wang^{*a}

^a*Department of Physics, The Chinese University of Hong Kong, Shatin, Hong Kong SAR, China. E-mail: xlzhuo@phy.cuhk.edu.hk; jfwang@phy.cuhk.edu.hk*

^b*CIC biomaGUNE, Basque Research and Technology Alliance (BRTA), 20014 Donostia–San Sebastián, Spain*

[‡]These authors contributed equally.

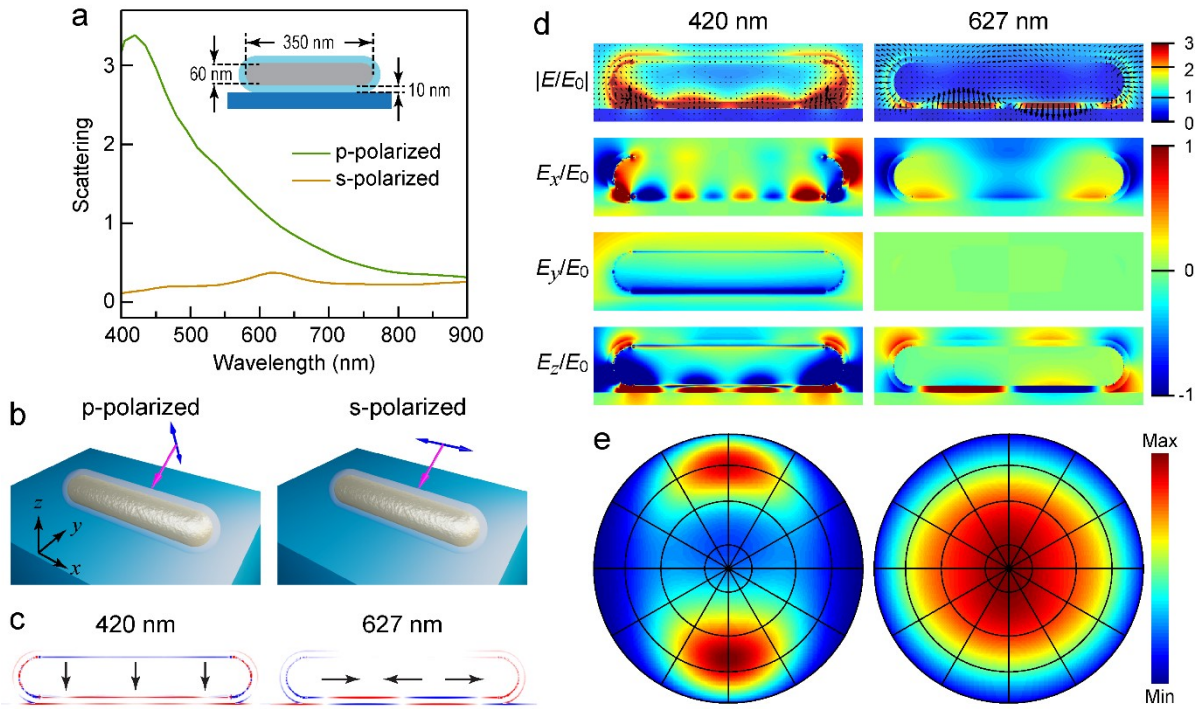


Fig. S1 Simulation results on the Si-supported (Ag NR)@mSiO₂ system with a gap distance of 10 nm under plane-wave excitation. (a) Simulated scattering spectra under the plane-wave excitation with p-/s-polarization and an incidence angle of 60° relative to the surface normal. The inset shows the simulation model with the values of the geometrical parameters. (b) Schematics of the p-/s-polarized excitation schemes. (c–e) Simulated charge distribution profiles (c), electric field enhancement profiles (d), and far-field patterns of the backward scattered light (e) under plane-wave excitation at 420 nm (p-polarized) and 627 nm (s-polarized), respectively. In the far-field patterns, the horizontal and vertical polar axes are along the longitudinal and transverse directions of the Ag NR, respectively. The radial axes, including the central point and the four circles from inside to outside, represent 0°, 10°, 30°, 60°, and 90° relative to the surface normal from the top view, respectively.

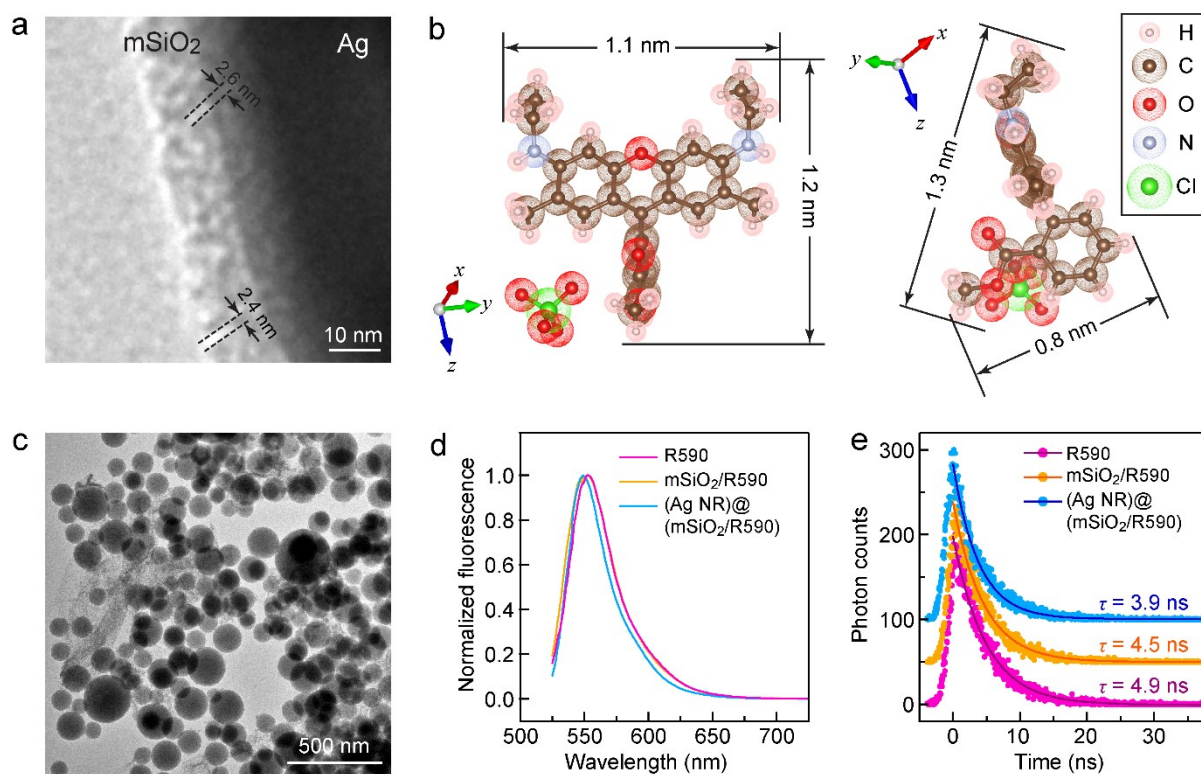


Fig. S2 Embedding of R590 in mSiO₂. (a) High-magnification TEM image of a (Ag NR)@(mSiO₂/R590) sample. The pore size of ~3 nm is roughly consistent with the value of ~4 nm reported in a previous work.¹ (b) Three-dimensional molecular structure of R590 (C₂₇H₂₉N₂ClO₇) at different angles.² Reproduced with permission.² Copyright 2016, Royal Society of Chemistry. (c) TEM image of the mSiO₂/R590 sample. The average diameter of the mSiO₂ nanospheres is 135 ± 50 nm. (d) Fluorescence emission spectra of the R590 solution, the mSiO₂/R590 sample, and the (Ag NR)@(mSiO₂/R590) sample. (e) Fluorescence decays of the three samples with offsets along the y-axis. Above each curve is the corresponding fluorescence lifetime, τ, obtained from fitting the experimental data (dots) with single exponential decay (line). All samples were measured in ethanol solutions with the excitation wavelength set at 514 nm.

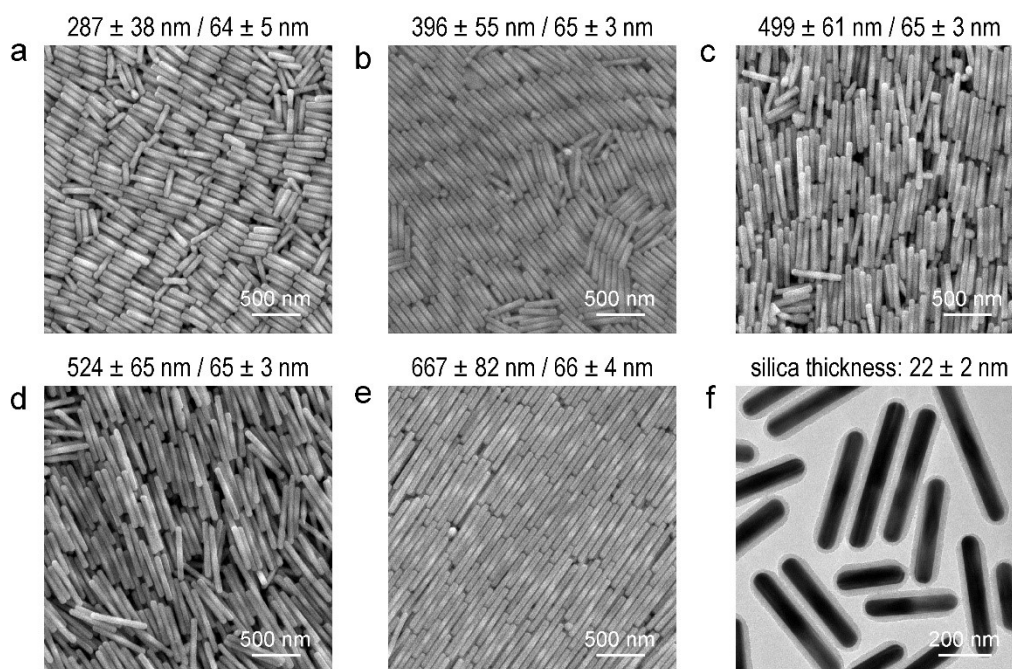


Fig. S3 SEM and TEM images of the Ag NR and (Ag NR)@(mSiO₂/R590) samples. (a–e) SEM images of five Ag NR samples with varied lengths and a fixed average diameter of ~65 nm. The numbers above each image are the average length and diameter of the corresponding Ag NR sample with standard deviations. (f) TEM image of the (Ag NR)@(mSiO₂/R590) sample used in the length-dependent experiment. The SiO₂ coating was performed for a mixture of the five Ag NR samples of different lengths, which guaranteed the uniformity of the silica thickness and the number density of the embedded R590 molecules.

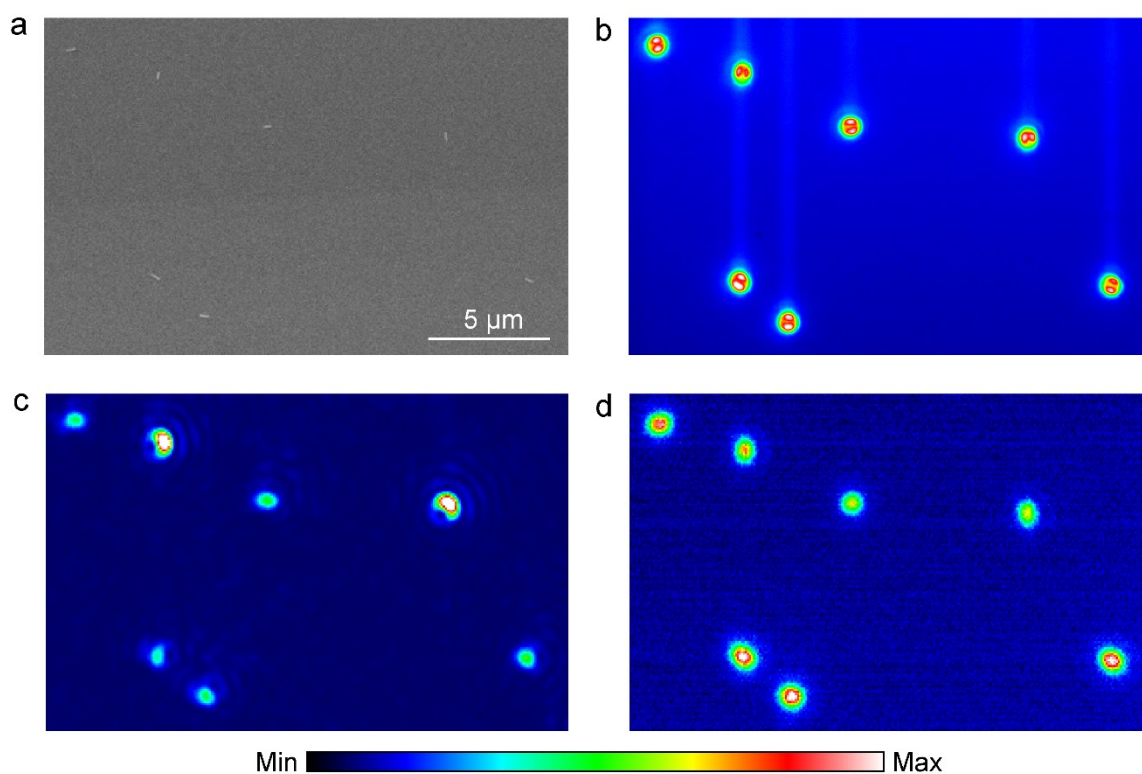


Fig. S4 Pattern-matching method for the single-particle measurements. (a) SEM image of a target area with seven single (Ag NR)@(mSiO₂/R590) nanostructures. (b) Dark-field scattering image of the same area under white-light excitation. A 100× dark-field objective (NA: 0.9) was employed. It provides an incidence angle of 64° relative to the surface normal. (c) Dark-field image of the same area under the excitation of a 514 nm laser at an incidence angle of ~60° relative to the surface normal. A 50× dark-field objective (NA: 0.5) was used for collecting the combined signals of scattering and fluorescence. (d) Corresponding fluorescence image with a 530 nm long-pass filter inserted in front of the camera. The filter blocked the scattering signal of the 514 nm laser and allowed the fluorescence signal from each nanostructure to pass through.

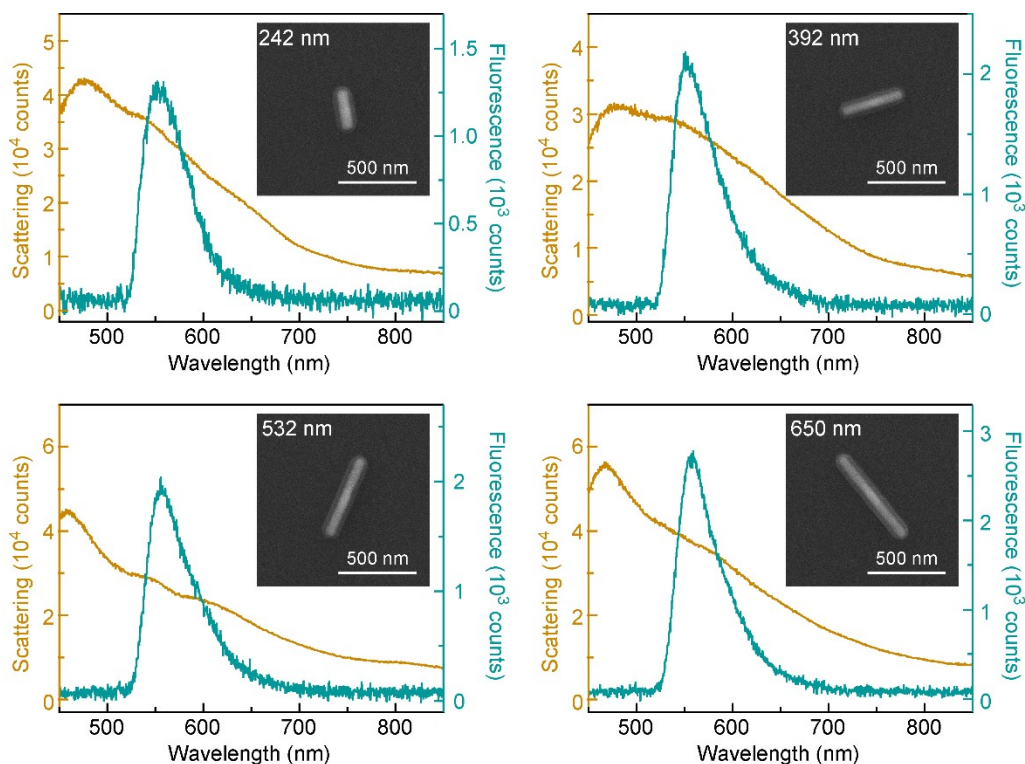


Fig. S5 Dark-field scattering and fluorescence spectra of four representative (Ag NR) $@(mSiO_2/R590)$ nanostructures with different lengths. The length of each Ag NR is given in the SEM image in the inset. The diameters of all Ag NRs are ~ 65 nm.

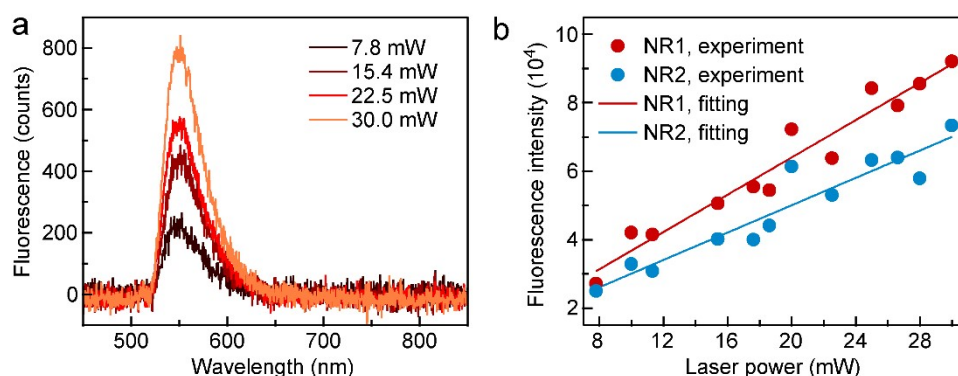


Fig. S6 Power-dependent measurements of the single-particle fluorescence. (a) Fluorescence spectra of a single (Ag NR) $@(mSiO_2/R590)$ nanostructure under the excitation of the 514 nm laser at different powers. (b) Power-dependent fluorescence intensities of two representative (Ag NR) $@(mSiO_2/R590)$ nanostructures. Each data point is an integral of a single-particle fluorescence spectrum from 500 nm to 660 nm. The lines represent the linear fitting results of the data points. The coefficients of determination (R^2) for the linear fitting are 0.94 for NR1 and 0.89 for NR2.

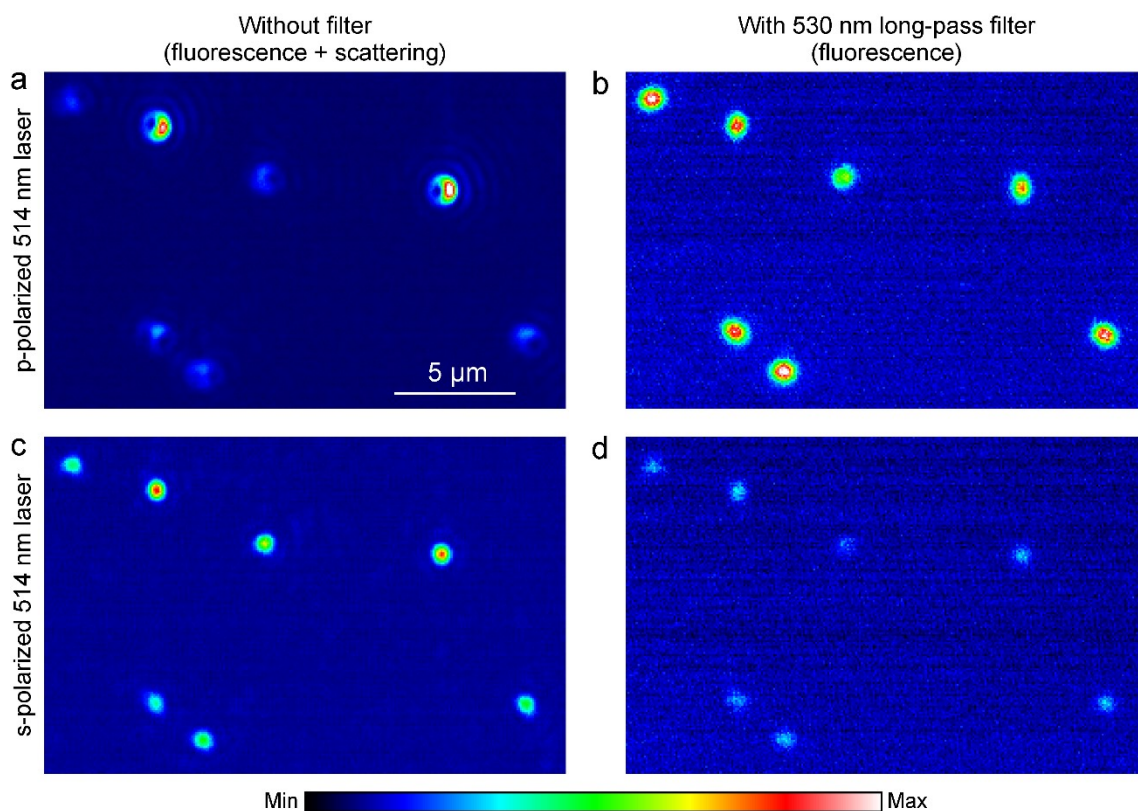


Fig. S7 Single-particle images under the excitation of the p- and s-polarized 514 nm laser light with the same intensity, using a fixed exposure time of 1 s for imaging. The images without the 530 nm long-pass filter are a combination of the scattered laser light and fluorescence emission signals. The images with the filter contain the fluorescence signal only. The SEM image of the target area has been provided in Fig. S4a. (a and b) Single-particle images under the excitation of the p-polarized laser light without/with the filter. The hollow patterns in (a) are the typical characteristics for the excitation of the broadside plasmon mode. (c and d) Single-particle images under the excitation of the s-polarized laser light without/with the filter. Although the fluorescence images were observable under the excitation of the s-polarized laser light, their intensities were too weak for detection in the spectral measurements.

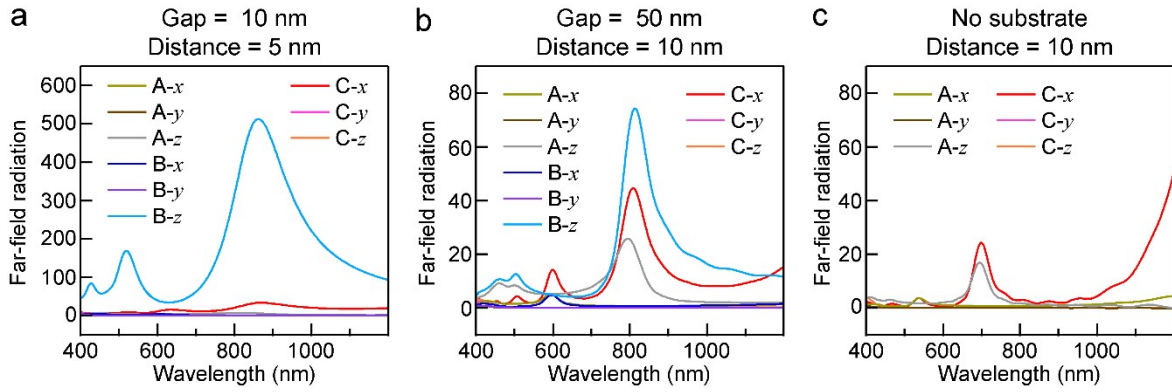


Fig. S8 Far-field radiation spectra from a single electric dipole coupled to a single Ag NR under different conditions. The x -, y - or z -oriented dipoles were set above (A), below (B) or at one end of (C) a Ag NR with the length/diameter of 350 nm/60 nm. The geometrical parameters of each model are given above each plot. (a) Spectra obtained from the single dipoles coupled to the Si-supported Ag NR with a fixed SiO₂ thickness of 10 nm and a fixed dipole–NR distance of 5 nm. (b) Spectra obtained from the single dipoles coupled to the Si-supported Ag NR with a fixed SiO₂ thickness of 50 nm and a fixed dipole–NR distance of 10 nm. (c) Spectra obtained from the single dipoles coupled to the free-standing Ag NR with a fixed SiO₂ thickness of 20 nm and a fixed dipole–NR distance of 10 nm.

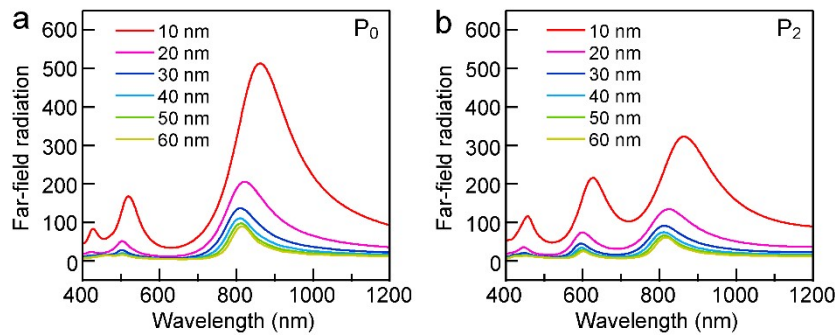


Fig. S9 Far-field radiation spectra obtained from the z -oriented dipoles at the position P₀ (a) and P₂ (b) of the Si-supported Ag NR (length/diameter: 350 nm/60 nm, SiO₂ thickness: 10–60 nm), with a fixed dipole–NR distance of 5 nm. The definitions of P₀ and P₂ are the same as those in Fig. 4b.

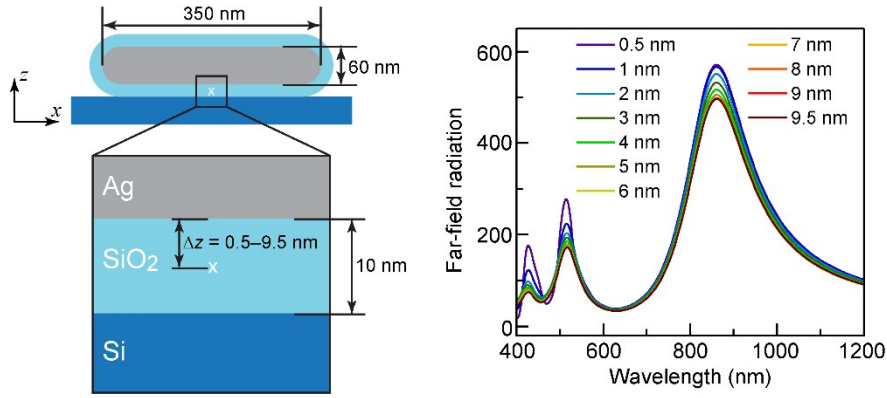


Fig. S10 Far-field radiation spectra obtained from the z -oriented dipoles with varied distances to the Ag surface, with the gap distance fixed at 10 nm. The single dipoles were set at $\Delta z = 0.5\text{--}9.5$ nm away from the Ag NR surface. In the case of $\Delta z = 9.5$ nm, the dipole can be approximately regarded as being located at the $\text{SiO}_2\text{--Si}$ interface. This result suggests that the insertion of a thin layer of nano-emitters at the $\text{SiO}_2\text{--Si}$ interface, such as the introduction of some two-dimensional luminescent materials, can be a promising alternative approach to this design.

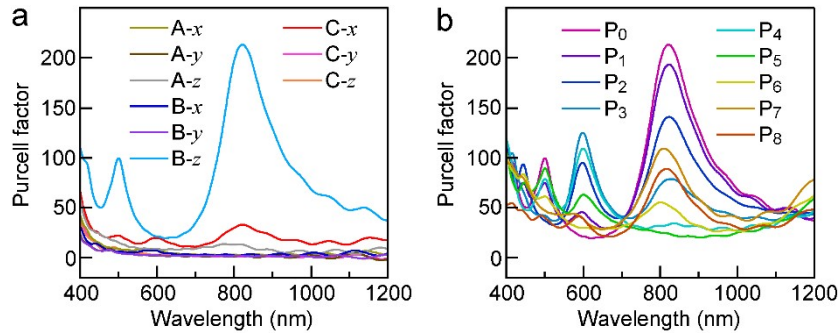


Fig. S11 Purcell factors calculated under different conditions. (a) Purcell factors obtained from the x -, y - or z -oriented dipoles above (A), below (B) or at one end of (C) the Ag NR (length/diameter: 350 nm/60 nm, SiO_2 thickness: 20 nm), corresponding to the far-field radiation spectra shown in Fig. 4a. (b) Purcell factors obtained from the z -oriented dipole at different positions ($P_0\text{--}P_8$) in the gap region, corresponding to the far-field radiation spectra shown in Fig. 4b.

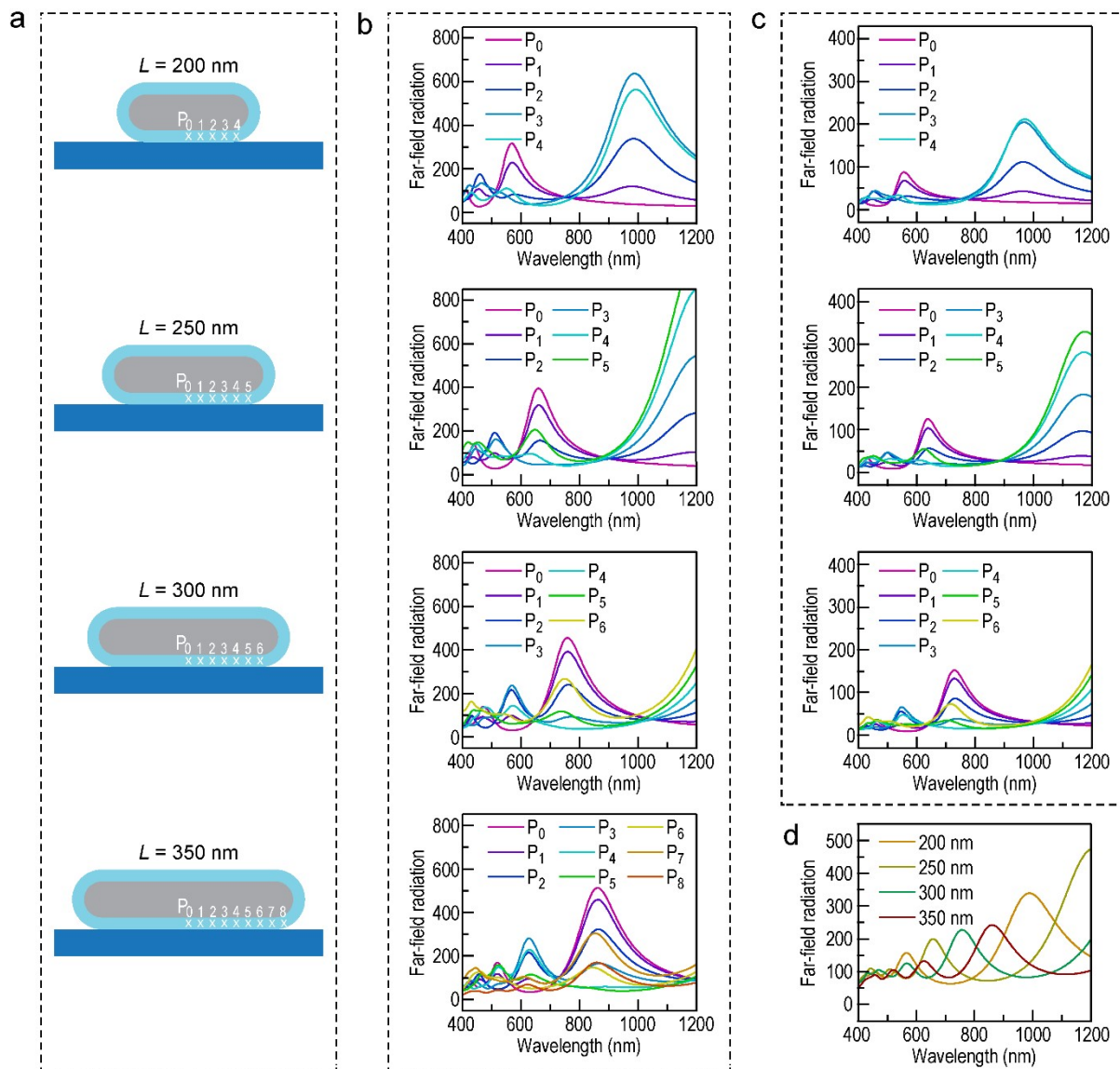


Fig. S12 Effect of the Ag NR length on the emission of the z -oriented dipoles sitting in the gap region. (a) Schematics of the simulation models with different Ag NR lengths. P_0 – P_8 have a distance of 20 nm to their nearest neighbors, with P_0 sitting at the middle relative to the Ag NR. The single dipoles were set at 10 nm away from the Ag NR surface. (b) Far-field radiation spectra obtained from the z -oriented dipoles coupled to the single Ag NRs with different lengths, with the gap distance fixed at 10 nm. From top to bottom are the results for the Ag NRs with lengths of 200 nm, 250 nm, 300 nm, and 350 nm, respectively. (c) Far-field radiation spectra obtained from the z -oriented dipoles coupled to the single Ag NRs of the different lengths, with the gap distance fixed at 20 nm. From top to bottom are the results for the Ag NRs of 200 nm, 250 nm, and 300 nm. (d) Averaged far-field radiation spectra obtained from the single Ag NRs with varied lengths of 200–350 nm and a fixed gap distance of 10 nm. Each spectrum is an average among the z -oriented dipoles at different positions.

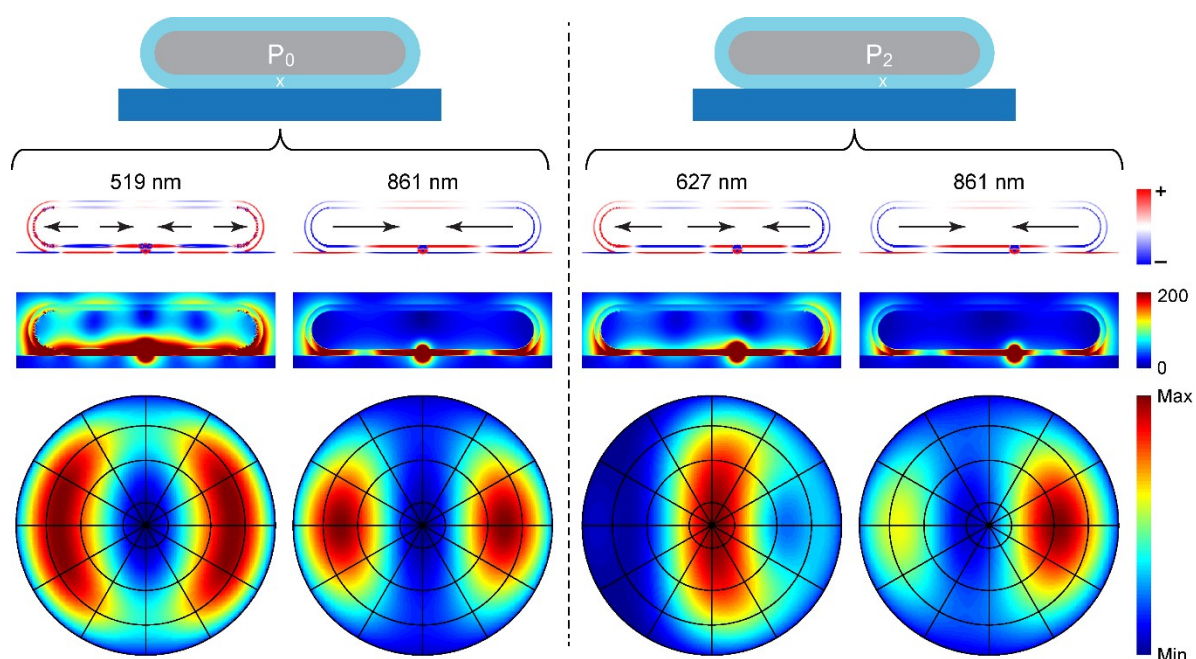


Fig. S13 Near- and far-field profiles at the plasmon resonance wavelengths of the 350 nm Ag NR with the gap distance (SiO_2 thickness) of 10 nm. The single dipole was set at 10 nm away from the Ag NR surface. The plasmon modes with their resonance wavelengths at 519 nm, 627 nm, and 861 nm are the hexadecapole ($N = 4$), octupole ($N = 3$), and quadrupole ($N = 2$) plasmon modes, respectively. From top to bottom rows are the schematics of the simulation models, charge distribution profiles, electric field profiles, and angular far-field radiation patterns. The polar axes of the far-field patterns are defined the same as those in Fig. S1.

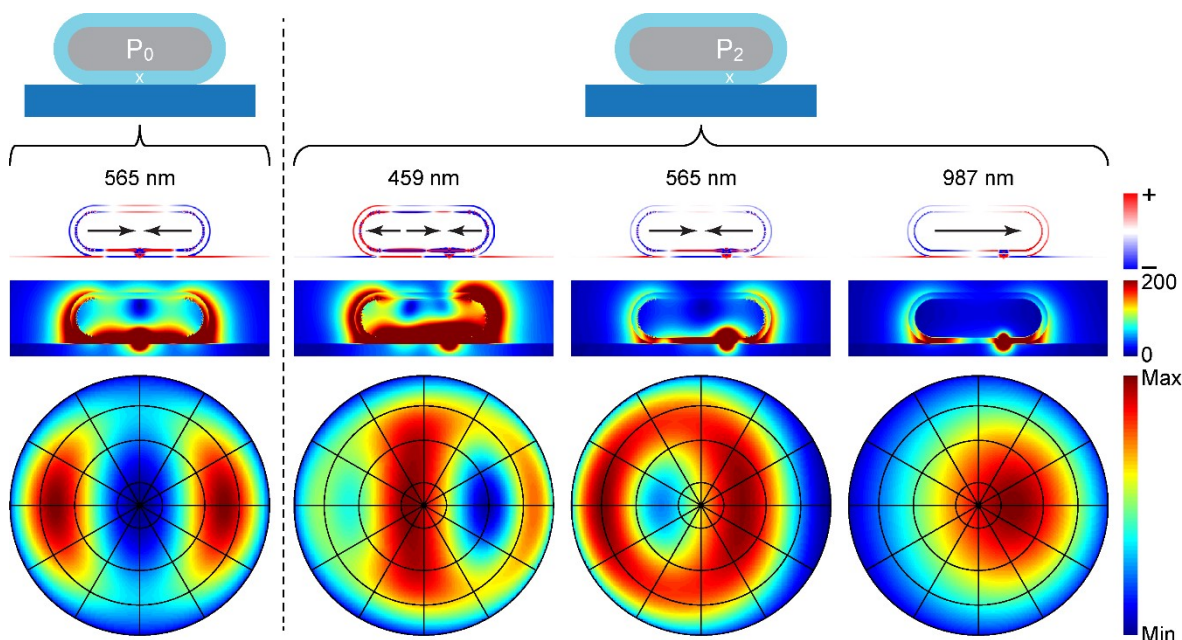


Fig. S14 Near- and far-field profiles at the plasmon resonance wavelengths of the 200 nm Ag NR with the gap distance (SiO_2 thickness) of 10 nm. The single dipole was set at 10 nm away from the Ag NR surface. The plasmon modes with their resonance wavelengths at 459 nm, 565 nm, and 987 nm are the octupole ($N=3$), quadrupole ($N=2$), and dipole ($N=1$) plasmon modes, respectively. From top to bottom rows are the schematics of the simulation models, charge distribution profiles, electric field profiles, and angular far-field radiation patterns. The polar axes of the far-field patterns are defined the same as those in Fig. S1.

References

- 1 Gorelikov and N. Matsuura, *Nano Lett.*, 2008, **8**, 369–373.
- 2 G. Pepe, J. M. Cole, P. G. Waddell and J. I. Perry, *Mol. Syst. Des. Eng.*, 2016, **1**, 416–435.